POLITECNICO DI TORINO
Repository ISTITUZIONALE

Dimethyl sulphide poisoning of a Ni-anode SOFC stack: concentration dependence and reversibility

Original
Dimethyl sulphide poisoning of a Ni-anode SOFC stack: concentration dependence and reversibility / Pera, L., Wesoly, A., Diethelm, S., Frantz, C., Yu, H., Gandiglio, M., Marocco, P., Santarelli, M., Van Herle, J.. - In: JOURNAL OF POWER SOURCES. - ISSN 0378-7753. - 694:(2026). [10.1016/j.jpowsour.2026.241255]

Availability:
This version is available at: 11583/3014867 since: 2026-08-26T06:19:15Z

Publisher:
Elsevier

Published
DOI:10.1016/j.jpowsour.2026.241255

Terms of use:

This article is made available under terms and conditions as specified in the corresponding bibliographic description in the repository

Publisher copyright

(Article begins on next page)

17 October 2026

Journal of Power Sources 694 (2026) 241255

Contents lists available at ScienceDirect

Journal of Power Sources

journal homepage: www.elsevier.com/locate/jpowsour

Dimethyl sulphide poisoning of a Ni-anode SOFC stack: concentration dependence and reversibility

Lucia Pera [a,b,*], Audrey Wesoly [b], Stefan Diethelm [c], Cédric Frantz [b], Hangyu Yu [b,**], Marta Gandiglio [a], Paolo Marocco [a], Massimo Santarelli [a], Jan Van Herle [b]

[a] Department of Energy, Politecnico di Torino, Corso Duca degli Abruzzi 24, Torino, 10129, Italy
[b] Group of Energy Materials, Swiss Federal Institute of Technology in Lausanne (EPFL), Rue de l'Industrie 17, Sion, Valais, 1950, Switzerland
[c] SolydEra SA, av. Des Sports 26, Yverdon-les-Bains, 1400, Switzerland

HIGHLIGHTS

- DMS poisoning investigated in a six-cell SOFC short stack.
- DMS exposure under load causes concentration- and time-dependent losses.
- EIS, DRT and ECM identify the main affected processes.
- DMS-induced degradation is largely reversible after contaminant removal.
- Sulphur coverage correlates linearly with voltage loss under load.

GRAPHICAL ABSTRACT

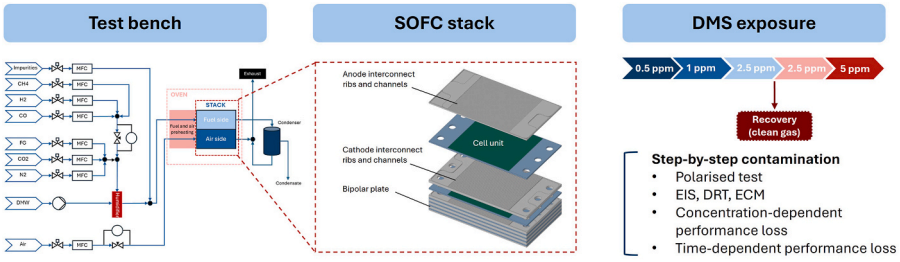

ARTICLE INFO

Keywords:
Solid oxide fuel cell stack
Dimethyl sulphide
Poisoning reversibility
Electrochemical impedance spectroscopy
Sulphur coverage

ABSTRACT

Biomass-derived fuels enable low-carbon power generation through solid oxide fuel cells (SOFCs); however, sulphur species present in biogas can severely degrade Ni-based anodes. Although H_2S poisoning has been extensively studied in single cells, the impact of other sulphur compounds at stack level and realistic load conditions remains poorly understood.

This study exposes a six-cell Ni-anode SOFC short stack to dimethyl sulphide (DMS) under biogas-relevant conditions, probing degradation through IV curves, electrochemical impedance spectroscopy (EIS), distribution of relaxation times (DRT) analysis, and equivalent circuit modelling (ECM). Tests were performed at 750°C, 0.4 Acm^{-2} and 65% fuel utilisation.

Under load, DMS poisoning (0.5, 1, 2.5 and 5 ppm) reveals voltage degradation trends consistent with concentration- and time-dependence, though not fully separable from exposure history. Electrochemical analysis shows that the anode charge-transfer process is selectively and substantially impaired, while gas-diffusion impedance evolves more gradually. Recovery upon contaminant removal confirms this degradation remains largely reversible within the investigated time window. Sulphur surface coverage, estimated using a Temkin-type adsorption model, correlates linearly with voltage loss, suggesting a coverage threshold of almost 0.7, below

* Corresponding author. Politecnico di Torino, Italy.
** Corresponding author. Swiss Federal Institute of Technology in Lausanne (EPFL), Switzerland.
E-mail addresses: lucia.pera@polito.it (L. Pera), hangyu.yu@epfl.ch (H. Yu).

https://doi.org/10.1016/j.jpowsour.2026.241255
Received 29 May 2026; Received in revised form 3 August 2026; Accepted 12 August 2026
Available online 25 August 2026
0378-7753/© 2026 The Authors. Published by Elsevier B.V. This is an open access article under the CC BY license (http://creativecommons.org/licenses/by/4.0/).

which degradation remains negligible. Together, these operando descriptors provide a preliminary, model-dependent framework for interpreting DMS poisoning trends at stack scale.

1. Introduction

Solid Oxide Fuel Cells (SOFC) are high-temperature electrochemical energy devices that directly convert the chemical energy of a fuel into electricity and useful heat [1]. SOFCs exhibit exceptional fuel flexibility and can electrochemically oxidise not only hydrogen but also carbon monoxide, while hydrocarbons such as methane may be internally reformed and then electrochemically utilized. This versatility makes SOFCs particularly attractive for integration with biomass-derived fuels (biogas and bio-syngas), which have been widely investigated as potential feeds for SOFC systems [2,3]. Several studies have reported high electrical efficiencies for SOFCs operating on such fuels, approaching 55% [4,5], highlighting their potential as efficient conversion technologies for renewable gaseous resources.

Despite these advantages, the practical use of bio-syngas is strongly constrained by the presence of trace contaminants, which can adversely affect both catalytic reforming reactions and electrochemical activity at the anode. Among the various impurities, sulphur-containing species are generally regarded as the most detrimental [6], including hydrogen sulphide (H_2S), carbonyl sulphide (COS), dimethyl sulphide (DMS), mercaptans, and thiophenes. Their concentrations depend on feedstock type, gasification and clean-up pathway, and operating conditions: H_2S can span a very wide range up to hundreds or even thousands of ppm in poorly cleaned streams, whereas other sulphur-compounds are often present at lower levels but may still cause significant performance losses even at sub-ppm concentrations [7,8].

Most of the available literature on sulphur poisoning in Ni-based SOFC anodes has focused on H_2S [9–13], which is often used as a model contaminant due to its prevalence in practical gas streams. As a result, a number of mechanistic and semi-empirical descriptions have been developed primarily for H_2S, linking performance losses to sulphur concentration and recovery [14–16].

Sulphur poisoning of Ni-based SOFC anodes is often described as a two-stage process [17–19]. A first, rapid degradation phase is typically observed immediately after H_2S introduction and is commonly attributed to the dissociative chemisorption of H_2S on nickel, which forms adsorbed sulphur species that progressively occupy electrochemically active Ni sites. This surface coverage reduces the availability of reaction sites at or near the triple-phase boundary (TPB), thereby increasing the anode polarisation losses associated with fuel oxidation.

At longer exposure times and sufficiently high sulphur activities, a second, slower degradation regime may develop, which has been linked to the onset of bulk processes such as the formation of nickel sulphide phases (Ni_3S_x) and sulphur-induced microstructural changes [18]. These processes can alter the anode morphology and reduce the effective TPB length and percolation pathways, resulting in a more persistent performance decay. Importantly, the extent to which the anode behaviour is reversible depends strongly on operating conditions and exposure history: at low H_2S levels and short durations, performance recovery upon sulphur removal is frequently observed, whereas higher concentrations or prolonged exposure can lead to incomplete recovery consistent with deeper structural or phase-related changes [20].

Nevertheless, real biomass-derived fuels may also contain significant fractions of other sulphur species, whose poisoning behaviour can differ from that of H_2S because it may involve additional decomposition, reforming, or conversion steps before sulphur becomes available for adsorption on Ni. Among these compounds, some studies have investigated thiophene as a representative sulphur contaminant, reporting measurable performance degradation even at low concentrations and highlighting the role of operating conditions in governing both the kinetics and reversibility of poisoning [21,22].

DMS represents a particularly challenging case compared with H_2S because its poisoning action is not governed solely by a simple adsorption equilibrium at the anode and its presence leads to a remarkable degradation [23]. Yu et al. [24] have hypothesised a two-stage poisoning mechanism on Ni-GDC cells: firstly, the DMS covers the active sites on the GDC surface, then it cracks into H_2S and CH_4. The reaction between CH_4 and H_2O is preferred and hinders the adsorption of H_2S on the active sites, ensuring negligible irreversible degradation. Moreover, compared with the extensive body of work on H_2S, often conducted on single cells under well-defined conditions, systematic analysis of DMS poisoning in stack level remains more limited.

In this work we move beyond the H_2S centric view of sulphur poisoning by providing, to the best of our knowledge, one of the first systematic stack level datasets on DMS exposure, spanning multiple concentrations (0.5-5 ppm) under controlled operating conditions. The novelty is twofold. First, the contaminant investigated is an organo-sulphur species whose poisoning pathway is intrinsically less straightforward than H_2S, because it may involve in situ conversion before sulphur becomes available for adsorption on Ni; consequently, concentration alone is often an insufficient descriptor and reliable tolerance limits remain scarce. Second, experiments are carried out on a six-cell SOFC stack, rather than on a single cell, thereby capturing the practical features that dominate real operation. In addition, the work explicitly addresses the reversibility of DMS-induced losses by tracking performance recovery after contaminant removal. Finally, to enable comparison with established sulphur metrics while accounting for stack operating conditions, the results are interpreted through a Temkin-like effective sulphur coverage index, and a compact correlation between performance drop and sulphur coverage is proposed to identify onset thresholds and practical contaminant limits. Taken together, these elements provide a new experimental and modelling framework for DMS poisoning that is directly relevant to SOFC deployment on biomass-derived fuels.

2. Experimental set up

2.1. Test bench and cell configurations

The SOFC test bench is designed to supply the stack with well-controlled fuel mixtures, including optional contaminants, and a separately regulated air stream, while ensuring appropriate humidification and thermal conditioning before entry into the hot zone. On the fuel side, individual gas lines (e.g., H_2, CO, CH_4, CO_2, N_2, plus a dedicated impurities line for contaminant dosing) are each equipped with a shut-off valve and a mass flow controller (MFC), allowing the desired composition to be set by adjusting the corresponding flow rates. The metered streams are then combined in a common mixing manifold; the routing around the manifold includes valves and bypass sections used for line isolation, purging and operational switching. When steam is required, demineralized water is pumped to a humidifier placed on the fuel line, so that the inlet fuel can be delivered either dry or with a controlled water content. In parallel, the cathode supply is provided by an independent air line, also regulated by a valve and MFC to set the air flow rate. Fuel and air are subsequently fed to the furnace, where they pass through a preheating section to reach the target inlet temperature before entering the SOFC stack (fuel side/anode and air side/cathode). At the outlet, the exhaust stream is cooled in a condenser to remove water by condensation; the liquid is collected as condensate, while the remaining gas is routed to the exhaust line. A control unit of the test bench includes the computer, the uninterrupted power supply (UPS), the electronic load and the data acquisition.

The SolydEra short stack is the same as that the standardised SolydEra G8 stack, but it is composed of six anode-supported cells. The cells

are rectangular with an active area of 80 cm^2 (11.2 cm × 7.2 cm), where the fuel flow enters from the short side. Each cell exhibits a five-layer functional structure: Ni-YSZ/8YSZ/GDC/LSCF-GDC/LSC [25]. Seven voltage probes are welded on the six interconnects and on the top plate. As for the current collection, the negative and positive poles stand respectively outside and inside of the compression rods.

2.2. Test protocols

The fuel cell is operated in galvanostatic mode. After heat-up with a ramp between 60 and 100 °C/h, the six-cell short stack was operated at 750°C during the entire experimental campaign. The furnace heating rate was kept as low as possible to minimize the temperature difference between the furnace and the fuel cell during start-up, thereby reducing thermal stresses associated with temperature ramping. The stack is first qualified under reference conditions by recording an I-V curve and performing electrochemical impedance spectroscopy (EIS) measurements. The stack is then polarised at steady current to establish a baseline under cold recirculation before reformer (CB) condition, as reported in Table 1. The CB composition involves cold-drying of the recirculated anode off-gas, promoting dry reforming of methane and resulting in CO-rich reformate. The contamination phase is carried out following a step-by-step procedure in which the sulphur concentration is increased every 20-145 h.

Sulphur is introduced by injecting a controlled flow of a 500 ppm DMS in H_2 mixture through an additional mass flow controller. To keep the total inlet flow rate constant, the corresponding amount of hydrogen added via this line is compensated by reducing the setpoint of the main H_2 mass flow controller by the same amount. No contamination tests are performed under reference conditions. In general, I-V curves and EIS measurements are acquired before and after any change in operating conditions. I-V curves and EIS measurements were performed using a Zahner ZENNIUM X Electrochemical Workstation equipped with two PAD4 cards, enabling the simultaneous voltage measurement of the six individual cells, and an external EL1000 electronic load/potentiostat capable of supplying up to 1 kW. EIS spectra were acquired under galvanostatic conditions at an operating current density of 0.4 A cm^{-2}, by applying a sinusoidal current perturbation with an amplitude of 2 A over the frequency range from 200 kHz to 50 mHz.

The stack is tested for about 2500 h: it is first maintained in CB conditions to establish the baseline and then subjected to a short exposure (also referred to as “Langnickel exposure” inspired by Langnickel et al. [26]) at DMS concentrations of 0.5, 1, 2.5, and 5 ppm. However, since the focus of this work is on the step-by-step test, the short exposure details and results can be found in the Supplementary Information.

The stack is later exposed to a step-by-step contamination protocol under polarisation, as outlined in Fig. 1. After an initial baseline, the sulphur impact is tested under polarised conditions (32.5 A). The sulphur levels are 0.5, 1 and 2.5 ppm. Then a recovery phase follows and when the repeating unit potentials reaches the previous initial performance, the contamination is continued with 2.5 and 5 ppm of DMS. The stack temperatures and pressures also stay stable and constant.

3. Data analysis

The data analysis is organised in three sequential steps via the open-source software, SOCEIS. First, the raw impedance data are processed using the linear Kramers-Kronig (KK) method, following the methodology described in our previous work [27]. The validity of each spectrum is assessed through the KK residuals provided by the SOCEIS software. A maximum KK residual threshold of 1.0% is adopted as acceptance criterion. Spectra not fulfilling this requirement are inspected and corrected by removing isolated non-physical points associated with external disturbances. The remaining data are subsequently smoothed and completed through KK-based extrapolation to obtain a uniform dataset.

The second step concerned the distribution of relaxation times (DRT), reconstructed following the positive Tikhonov regularisation approach described by Boukamp [28] by minimizing:

$$x = \mathrm{argmin}\left(||Ax - b||^2 + \lambda^2||Lx||^2\right) \quad (1)$$

where the first term minimizes the residual between the measured and reconstructed impedance spectra, while the second term penalizes oscillatory solutions. The regularisation parameter (λ) controls the balance between fitting accuracy and smoothness of the reconstructed distribution.

The regularisation parameter was selected using the L-curve criterion, which identifies the optimal compromise between the residual norm and the norm of the regularised solution. Based on the range of optimal values obtained for the different spectra, a fixed value of $\lambda = 0.01$ was adopted throughout the study. This value provided a satisfactory compromise between excessive smoothing and noise amplification while ensuring consistent comparison of the DRT spectra under all operating conditions. Prior to DRT reconstruction, all impedance spectra were validated through the Kramers–Kronig consistency test, ensuring that only physically consistent spectra were analysed.

Finally, the equivalent circuit model (ECM) is defined based on the number of characteristic time-scale of the processes identified from the DRT (Fig. 2), using a corresponding set of RQ elements. The circuit parameters, such as process resistances, characteristic time constants, and dispersion factors, are then estimated by complex non-linear least-squares (CNLS) fitting of the impedance spectra with cross validation via DRT peak distribution.

4. Results and discussion

4.1. Voltage characterisation

As previously described, the step-by-step test protocol consists of sequential exposures to 0.5, 1 and 2.5 ppm of DMS, followed by a recovery phase, and finally a second exposure to 2.5 ppm and to 5 ppm. It should be noted that this is a stepped exposure protocol rather than a set of independent concentration-response tests: each contamination step (with the exception of the first) starts from a stack state already influenced by prior DMS exposure, recovery extent, and possible incremental ageing. As a result, concentration, exposure time, poisoning history, and recovery state are not fully separated in this dataset, and trends reported below with respect to DMS concentration should be interpreted as apparent trends observed within this sequential protocol rather than as an independently validated concentration-dependence law.

Fig. 3 reports the temporal evolution of the voltage of each of the six cells composing the stack during the different contamination and recovery phases.

Table 1
Gas compositions of the test conducted, including fuel utilisation (FU) and total inlet gas flow rates.

	Anode								Cathode		
	FU	H_2	CO	CO_2	H_2O	CH_4	N_2	Flow	AU	Air	Flow
	[%]	[%]	[%]	[%]	[%]	[%]	[%]	[NL/min]	[%]	[%]	[NL/min]
Ref cond.	75	60	-	-	-	-	40	2.879	17	100	32
CB	65	60	0	29	10	1	0	3.264	17	100	32

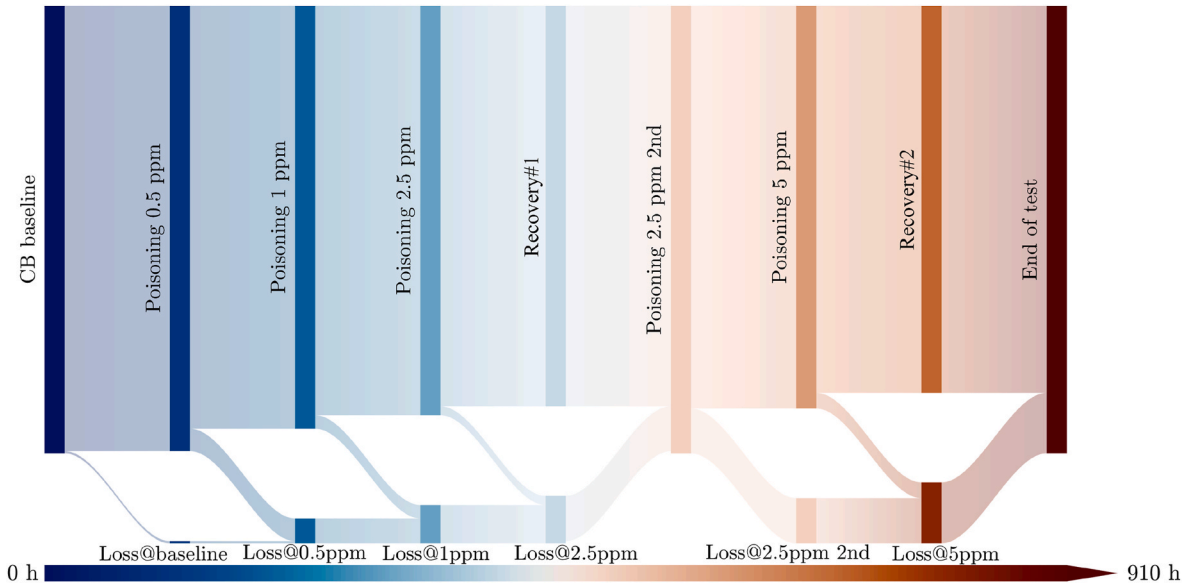

Fig. 1. Timeline of step-by-step degradation tests.

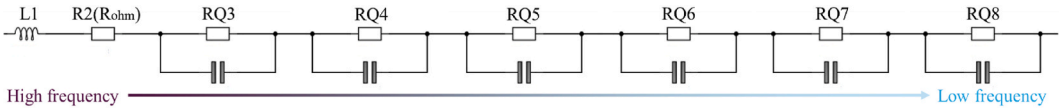

Fig. 2. Equivalent circuit model consisting of one inductor (L1), one resistor (R_{ohm} or R2), six RQ elements, where the bigger number corresponds to the lower frequency process.

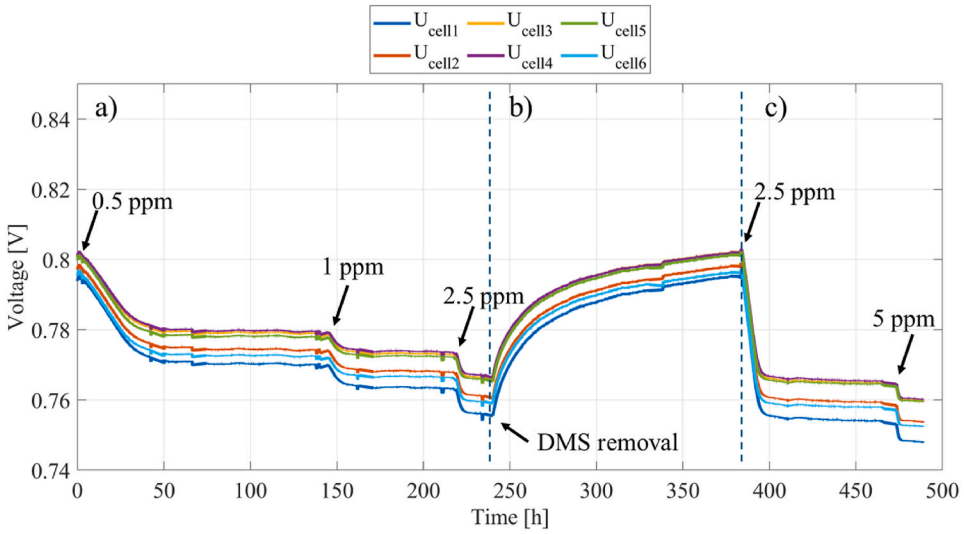

Fig. 3. Voltage trend for a) 0.5,1,2.5 ppm DMS exposure b) DMS removal, c) 2.5, 5 ppm DMS exposure.

The first introduction of 0.5 ppm results in the largest single-step voltage decrease. Once the system stabilizes and 1 ppm is injected, the additional voltage drop is significantly smaller. A similar behaviour is observed when increasing to 2.5 ppm. Despite the different degradation, in all three cases the voltage tends to stabilise at a new quasi-steady level, indicating that an equilibrium sulphur coverage is reached at each DMS concentration.

The following recovery phase, implemented between the two 2.5 ppm exposures, lasted approximately 150 h, as shown in Fig. 3b. During this period, the average stack voltage gradually recovered an average of 36.0 mV, eventually reaching the pre-contamination level before the subsequent contamination step. This complete restoration confirms that, within the investigated operating window, the degradation and voltage losses induced by DMS are predominantly reversible under the tested conditions.

The full recovery suggests that the dominant mechanism responsible for the initial exponential voltage drop is sulphur adsorption on active Ni sites, reducing the electrochemically active surface area. Upon DMS removal, sulphur species desorb and the active sites become available again, restoring the original electrochemical performance. No persistent electrochemical signature of irreversible degradation was detected within the investigated concentration range and exposure time, consistent with a

dominant reversible sulphur-adsorption mechanism rather than irreversible catalytic damage. As no post-test microstructural or phase characterisation was performed, subtle irreversible changes (e.g., Ni coarsening, local sulphide formation) cannot be excluded.

The second exposure at 2.5 ppm (after recovery #1) shows a markedly larger degradation. It should be noted that the voltage drops reported for each exposure step are evaluated relative to the voltage immediately preceding that specific step. Consequently, the first 2.5 ppm exposure, performed after the 1 ppm step, represents only the incremental response from an already partially poisoned state, whereas the later 2.5 ppm exposure starts from a different initial condition after recovery. For this reason, the two stepwise ΔV_{exp} values should not be interpreted as two independent repetitions of the same exposure from an identical initial electrode state.

Nevertheless, although this contamination starts from a higher initial stack potential due to voltage recovery, the final potentials reached in the two 2.5 ppm tests are comparable (762.7 mV and 761 mV). Moreover, the cumulative voltage loss at the end of the first 2.5 ppm exposure (34.3 mV) is only about 3 mV lower than the voltage loss measured in the second exposure. This indicates that, within the investigated experimental window, the final stack performance under a given sulphur level tends to converge towards a similar equilibrium value despite the different electrochemical state of the stack prior to contamination. Such behaviour supports the hypothesis that, at a fixed DMS concentration, a quasi-equilibrium sulphur coverage is reached. It should be noted, however, that this conclusion is based on the two 2.5 ppm exposure cycles investigated in the present work, and long-term irreversible degradation mechanisms may alter this behaviour over extended operating times.

For the final contamination stage at 5 ppm, it can be observed that the initial drop occurs rapidly, consistent with a faster surface coverage at higher sulphur partial pressure.

Recovery following the final 5 ppm exposure was also monitored via voltage, showing a substantial increase consistent with the reversible behaviour observed at lower concentrations (Figure S.1, Supplementary Information). However, this recovery phase was not characterised by EIS; complete electrochemical reversibility at 5 ppm should therefore be regarded as not fully confirmed by the present data.

For all contamination steps, the voltage evolution exhibits the characteristic behaviour already observed in cells exposed to sulphur compounds: an initial rapid, quasi-exponential voltage decay followed by a slower, approximately linear degradation regime. This two-stage response can be consistently identified at both stack and single-cell level, although the absolute voltage differs slightly among the six cells.

The initial exponential-like drop is here quantified by the parameter ΔV_{exp} and by the time required to reach this drop, which represents the duration of the transient regime before the onset of linear degradation. Physically, this stage is generally associated with the rapid adsorption of sulphur species on the active Ni sites, leading to a progressive reduction of the electrochemically active surface area. According to sulphur coverage theory, the voltage loss is expected to scale with the fraction of catalyst surface covered by sulphur, while the characteristic time of the drop is linked to the adsorption kinetics and contaminant concentration.

Fig. 3 shows that the time required to reach ΔV_{exp} decreases as the DMS concentration increases. For instance, 0.5 ppm leads to a 22.3 mV drop over 64 h, whereas 2.5 ppm (first exposure) produces a 6.4 mV drop in only 7 h, and 5 ppm causes a 5.1 mV drop within 6 h. This trend is consistent with faster surface coverage at higher sulphur partial pressure.

In addition, in order to provide a physically consistent descriptor of the transient degradation stage, the voltage drop was analysed using the time constant concept commonly adopted in control theory [29,30]. Assuming a first-order response, the time constant τ is defined as the time required for the voltage to reach the 63.2% of the total steady state drop. The transient voltage decay was described using a generalized two-term expression combining adsorption kinetics and linear degradation:

$$V(t) = V_0 - \Delta V_{exp}\left(1 - e^{-t/\tau}\right) - \delta_l \cdot t \quad (2)$$

where ΔV_{exp} represents the adsorption-driven voltage loss, τ the characteristic adsorption time constant, and δ_l the long-term linear degradation rate. The calculated τ values (see Table 2) decrease with increasing DMS concentration, confirming faster adsorption dynamics at higher DMS partial pressure. In particular, τ decreases markedly from the 0.5 ppm step to the 2.5 ppm exposure, highlighting the strong dependence of surface coverage kinetics on contaminant concentration.

Comparing the different contamination steps, it is evident that the first introduction of 0.5 ppm induces the largest single-step performance loss, whereas subsequent increases in concentration do not cause proportionally larger drops. After the first severe degradation observed at 0.5 ppm, subsequent exposures at 1 ppm and at the first 2.5 ppm level result in smaller ΔV_{exp} values (5.6 and 6.4 mV, respectively). This behaviour suggests that a fraction of the active sites might already be blocked or altered during the first contamination, reducing the number of sites available for further rapid poisoning. In other words, the system appears to approach a progressively lower "effective" active surface, so that additional sulphur causes a faster but not proportionally larger voltage drop.

After the initial drop, a linear degradation regime is observed. This stage is characterized by ΔV_{linear}, the exposure time, and the corresponding degradation rate (mV/kh). The linear regime is likely and partially irreversible degradation processes. Possible mechanisms include microstructural evolution of the fuel electrode, such as Ni coarsening, gradual loss of TPB length, or other cumulative chemical and morphological changes beyond simple reversible sulphur adsorption. Since no post-test microstructural characterization could be performed in the present work, these mechanisms should be regarded as plausible interpretations rather than direct experimental observations. The degradation rates vary significantly with concentration: from 7.5 mV/kh at 0.5 ppm up to 41.5 mV/kh at 5 ppm. The apparently high rate observed at the first 2.5 ppm level (33.3 mV/kh) is strongly influenced by the short exposure time (9 h), which amplifies the calculated slope. Within this stepped protocol, higher nominal DMS concentrations are associated with faster long-term linear degradation, although this trend cannot be fully isolated from exposure history.

Overall, the voltage characterisation is consistent with a two-stage degradation mechanism under DMS exposure: a fast adsorption-driven voltage drop, whose rate appears to increase with nominal DMS concentration within this stepped protocol, followed by a slower linear degradation likely associated with cumulative and partially irreversible processes.

Gas chromatography (GC) analysis of the anode outlet was performed. The analysis revealed that H_2S is consistently identified. This observation indicates that DMS undergoes decomposition leading to the formation of hydrogen sulphide as the active sulphur species reaching the anode. This finding supports the consistency of the poisoning behaviour with previously results on Ni-GDC electrolyte-supported cells, where DMS-induced performance loss is governed by reversible surface adsorption on nickel active sites [24].

4.2. Electrochemical impedance spectroscopy

The impedance spectra provide further insight into the mechanisms underlying the voltage behaviour observed during DMS exposure. In

Table 2
Mean potential loss during DMS exposure. Exponential and linear drops with corresponding times and time constants.

DMS concentration [ppm]	ΔV_{exp} [mV]	ΔV_{linear} [mV]	Linear degradation rate δ_l [mV/h]	Time constant τ [h]
0.5	21.6	0.7	7.5×10^{-3}	23.6
1	5.7	0.6	11.8×10^{-3}	5.1
2.5	6.4	0.3	33.3×10^{-3}[a]	2.5
2.5	36.2	0.7	12.3×10^{-3}	7.1
5	5.1	0.4	41.5×10^{-3}[a]	0.9

[a] Linear degradation to be considered indicative since the exposure lasted few hours.

Fig. 4a, the solid line represents the average stack response, while the shaded region corresponds to the envelope of the individual cell spectra. The latter is included to illustrate the cell-to-cell variability within the short stack and should not be interpreted as a statistical confidence interval or measurement uncertainty. During the first contamination sequence (0.5 → 1 → 2.5 ppm), a progressive enlargement of the high-frequency arc is clearly visible, accompanied by an increase in the low-frequency contribution, while the high-frequency intercept remains essentially unchanged. The stability of the ohmic resistance indicates that neither the electrolyte nor the electrical contacts are affected by the contaminant, confirming that the impact of DMS is confined to the electrode processes, primarily at the anode. The growth of the high-frequency arc is consistent with a reduction of the electrochemically active Ni surface due to sulphur adsorption, leading to an increase in anodic charge transfer resistance. More pronounced, however, is the enlargement of the low-frequency arc, which suggests a significant influence on processes coupled to gas conversion and chemical equilibria, such as the water-gas shift reaction. The inhibition of catalytic activity by sulphur likely alters the local gas composition and slows down chemical conversion, thereby amplifying mass-transport-related or conversion-related impedance contributions.

The recovery phase implemented between the two 2.5 ppm exposures provides decisive information on the reversibility of these effects (Fig. 4b). After DMS removal, the impedance spectrum returns almost completely to its pre-exposure shape, with both the high- and low-frequency arcs recovering to values comparable to the initial state and no detectable change in ohmic resistance. This behaviour demonstrates that the dominant degradation mechanism under the tested conditions is reversible sulphur poisoning rather than permanent structural damage. The data are therefore consistent with a dynamic adsorption-desorption process of sulphur species on Ni active sites, without significant loss of triple phase boundary or microstructural deterioration within the investigated exposure times.

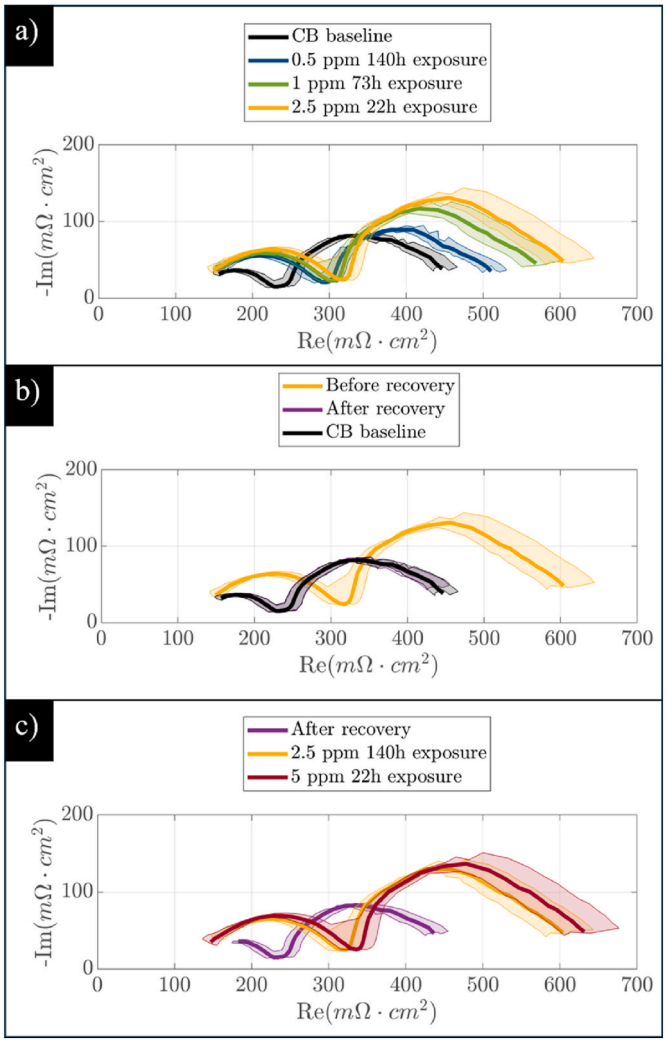

Fig. 4. EIS with mean value and error band for a) 0.5,1,2 ppm DMS exposure b) recovery phase, c) 2.5, 5 ppm DMS exposure.

During the subsequent re-exposure at 2.5 ppm and the final contamination at 5 ppm (Fig. 4c), the same qualitative behaviour is observed, but with a more pronounced increase in the low-frequency arc at higher concentration. In particular, the 5 ppm condition leads to a substantial enlargement of the low-frequency contribution, indicating that higher sulphur partial pressures intensify the limitation associated with gas conversion and coupled chemical reactions. The high-frequency region is also affected, though to a lesser extent, again pointing to surface site blocking as the primary mechanism. Overall, the EIS analysis corroborates the voltage characterisation results: DMS exposure induces an increase in anodic polarisation resistance that scales with nominal DMS concentration across the stepped protocol and it is dominated by reversible surface poisoning and by secondary effects on gas conversion kinetics, while the electrolyte and ohmic response of the stack show no measurable change within the explored operating window, indicating no persistent electrochemical signature of degradation at the cell-hardware level.

In addition to the average stack behaviour, the short-stack configuration allows the analysis of cell-to-cell variability along the fuel flow direction. Figure S.2. in Supplementary information reports a comparison of impedance spectra for selected cells located at different positions within the stack. A systematic trend is observed: the cell closest to the fuel inlet (cell 1) exhibits a larger increase in anodic polarisation resistance during DMS exposure compared to downstream cells. This behaviour is consistent with the higher sulphur partial pressure encountered at the inlet, prior to any conversion or dilution effects along the channel. This confirms that the degradation mechanism is directly linked to sulphur availability in the fuel stream and further supports the interpretation of adsorption-driven poisoning at the anode.

4.3. Distribution of relaxation times

The use of DRT as a complementary tool to conventional EIS analysis has attracted increasing attention because it enables the deconvolution of overlapping electrochemical processes without requiring an a priori equivalent circuit [31]. In contrast to the Nyquist representation, where overlapping arcs may mask the contribution of distinct mechanisms, the DRT deconvolution resolves the total polarisation resistance into discrete peaks, each associated with a characteristic relaxation time and therefore with a specific coupled process. Six recurrent peaks are consistently identified over the entire experimental campaign. Their attribution, summarised in Table 3, is based on a combination of literature interpretations [32,33], comparison with our previous single-cell investigations, and the physical consistency of the observed response to DMS poisoning. The proposed assignment is primarily based on the framework of Caliandro et al. [34]. In our previous Ni-YSZ single-cell study [25], the lowest-frequency contribution was attributed to gas conversion processes. However, the analysis of the present stack-level measurements suggests that the region below 10 Hz may contain two phenomena: intrinsic gas conversion and a slower conversion -diffusion contribution. In electrolyte-supported cell (ESC) configurations, where the fuel electrode is significantly thinner, the sub-hertz conversion-diffusion is often weak or not distinctly resolved, as reported for Ni-GDC based electrolyte-supported cells by Yu et al. [27]. In such systems, the low-frequency region is typically dominated by intrinsic gas conversion. In contrast, in anode-supported cells and, even more, at stack level, the thicker porous anode enhances spatial concentration gradients and chemical-electrochemical coupling, leading to the emergence of a slower conversion-diffusion process that becomes experimentally distinguishable

Table 3
Peaks classification for different electrochemical processes.

	P8	P7	P6	P5	P4	P3
Process	WGS conversion-diffusion at low p_{O_2} transport	Gas conversion	Fuel electrode diffusion and oxygen electrode reaction	Oxygen electrode transport and oxygen charge transfer	Fuel electrode charge transfer	Solid state process
Frequency	0.05-0.5 Hz	0.5-10 Hz	10-50 Hz	50-500 Hz	0.5-5 kHz	>5 kHz
Related electrodes	Anode	Anode	Anode and cathode	Cathode	Anode	Electrolyte

from intrinsic gas conversion. The proposed assignments are consistent with additional dedicated gas-composition experiments performed by the authors. Since those experiments are part of a separate study specifically devoted to peak attribution, they are not discussed further here.

Here, the lowest-frequency contribution (P8, 0.05-0.5 Hz) is attributed to a fuel-side water-gas shift (WGS) conversion-diffusion process associated with coupled electrochemical consumption and internal chemical equilibration in reforming mixture. In fact, under current load, at the anode TPB the electrochemical reactions consume reducing species and consequently the local oxygen chemical potential increases because H_2O and CO_2 are produced. On the other side, chemical reactions such as the WGS and the diffusion of species through the porous anode act to restore equilibrium. Chemical reactions and diffusion in porous media are slow processes with large characteristic times; in particular, the mass transfer of CO toward the electrode interphase is expected to be rate-limiting, since the diffusion coefficient of CO is significantly lower than that of H_2 (due to its higher molecular mass and collision diameter). Therefore, their relaxation time corresponds to frequencies typically below 1 Hz [35].

The adjacent low-frequency peak (P7, 0.5-10 Hz) is associated with gas conversion phenomena at the fuel electrode. This process reflects the coupling between electrochemical hydrogen consumption and the replenishment of reactants through internal reforming and chemical conversion. Variations in this peak indicate changes in the effective catalytic activity and in the ability of the electrode to maintain local equilibrium under load. Because sulphur adsorption reduces the number of active sites available for heterogeneous reactions, this contribution is expected to be strongly influenced by DMS presence.

In the intermediate frequency domain (P6, 10-100 Hz), the peak is attributed to fuel-electrode gas diffusion combined with oxygen-electrode surface reaction kinetics. The mixed attribution arises from the partial overlap of time constants in this region. On the fuel side, diffusion limitations within the porous structure and through the boundary layer contribute to the impedance response, while on the air side the surface exchange reaction may exhibit comparable characteristic times. The sensitivity of P6 to contamination is therefore indicative of indirect effects of sulphur poisoning on mass transport and interfacial reaction rates rather than on bulk ionic transport. Although P5 cannot be clearly resolved as an independent peak in the DRT spectra, previous single cells investigations [25,34] have consistently located this contribution in the 50-500 Hz range. In the current analysis, it most likely appears as a shoulder or as a broadening of the P6 feature, reflecting overlapping processes with partially similar time constants. Based on its characteristic frequency domain and earlier experimental evidence, P5 is tentatively associated with oxygen electrode transport and charge-transfer phenomena. The statistical justification for retaining a dedicated element for this contribution, together with the associated parameter uncertainty, is reported in the Supplementary Information.

At higher frequencies, P4 (0.5-5 kHz) is assigned to fuel-electrode charge transfer. This process corresponds to the electrochemical oxidation of hydrogen at the triple phase boundary and is directly linked to the density of active Ni sites. Sulphur adsorption reduces the effective active area, leading to an increase in the associated polarisation resistance.

Finally, the highest-frequency contribution (P3, >5 kHz) is attributed to solid-state processes, mainly charge accumulation or depletion at solid-solid interfaces and possibly fast interfacial phenomena at the electrode-electrolyte interface. The relatively high frequency and typically limited sensitivity of this peak to fuel composition confirm that it is largely independent of sulphur poisoning and instead governed by intrinsic material properties.

The peak assignments summarised in Table 3 represent our proposed interpretation of the DRT/CNLS results, consistent with the observed electrochemical behaviour, the equivalent circuit analysis, and comparison with previous single-cell studies, rather than a definitive identification of each individual process.

The DRT analysis allows the evolution of the individual electrochemical processes to be followed more clearly than in the Nyquist representation. Fig. 5 shows the DRT results for the three steps. As for EIS graph, the solid line represents the average DRT response of the six cells, whereas the shaded region encompasses the individual responses measured on each cell.

When DMS is introduced at 0.5 ppm, the peaks that show the most pronounced change are those associated with gas conversion (P7) and anode charge transfer (P4). Even at this relatively low concentration, sulphur species can adsorb on the Ni surface and form nickel-sulphur bonds, which reduce the catalytic activity of the fuel electrode. As the most active sites of the electrode become progressively blocked, the electrochemical oxidation of the fuel becomes less efficient and the charge transfer resistance increases. This contribution, represented by P4, is generally attributed to the kinetics of the electrochemical reactions occurring at the triple phase boundary. When sulphur covers part of the Ni surface, the density of available reaction sites decreases, forcing the electrochemical reaction to occur on a smaller active area. As a consequence, the effective path for ionic and electronic transport toward the remaining active sites becomes longer and the associated activation polarisation increases [16]. This evidence is coherent with the study of Madi et al. [22], who found that another sulphur compound (thiophene) mainly affected the high frequency relaxation process around 500 Hz, attributed to the charge transfer process.

At the same time, the gas conversion peak (P7) also increases noticeably. This behaviour can be explained by the strong coupling between electrochemical fuel consumption and catalytic reactions occurring at the anode, such as the water–gas shift reaction and other gas conversion processes that maintain the local equilibrium of the fuel mixture. When sulphur species adsorb on Ni, the catalytic activity of the electrode for these reactions is reduced. As a result, the gas mixture cannot rapidly re-equilibrate to compensate for the electrochemical consumption of hydrogen and carbon monoxide at the triple phase boundary. Sulphur poisoning modifies the kinetics of the existing gas-conversion process by reducing the catalytic activity of the Ni surface and altering the local $H_2/H_2O/CO/CO_2$ composition. Consequently, the increase in P7 is interpreted as an amplification of the intrinsic gas-conversion resistance. When the DMS concentration is increased from 0.5 ppm to 1 ppm and subsequently to 2.5 ppm, the same processes remain dominant. The height of P7 continues to increase, although the change becomes progressively smaller at higher concentrations. In contrast, P4 remains approximately constant after the first contamination step. This suggests that the initial exposure to sulphur already blocks a significant fraction of the most active catalytic sites on the Ni surface. Further increases in contaminant concentration therefore do not substantially increase the intrinsic charge transfer resistance, as the electrochemical reaction has already adapted to the reduced active area. Instead, additional sulphur primarily affects processes linked to gas-

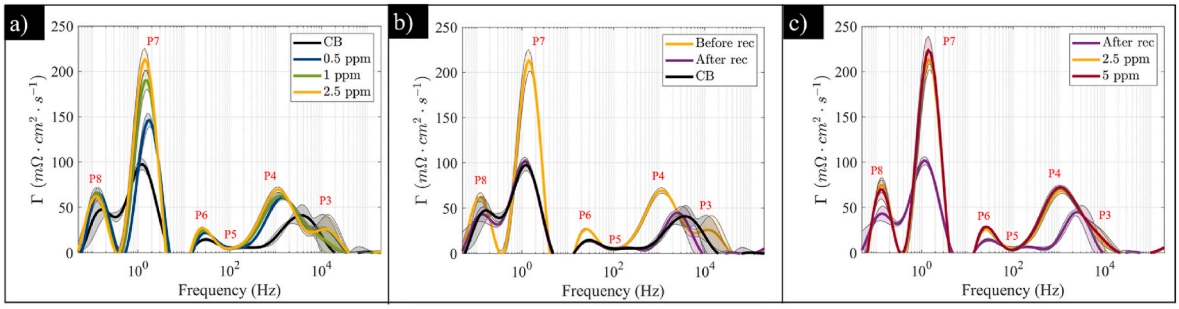

Fig. 5. DRT results with peak recognition to compare the behaviour of different contaminant concentrations. All measurements are taken before switching the contaminant composition.

phase conversion and chemical equilibrium within the porous electrode. A small increase is also observed for the lowest-frequency peak. Since this process depends on the catalytic activity and gas transport, the presence of sulphur can indirectly affect it slowing down the chemical reactions that assures equilibrium in the mixture and increasing the related resistance. Similarly, also in the intermediate-frequency peak P6 a moderate increase is detected. The slight increase suggests that the modification of the catalytic activity and the consequent change of the local gas composition may influence mass transport within the anode.

The recovery phase provides further confirmation of the reversible nature of the poisoning mechanism. As already observed in the EIS analysis, the DRT spectrum measured after DMS removal overlaps almost perfectly with the initial curve obtained before any contamination. All peaks return to their original magnitude and position, indicating that the electrochemical processes are fully restored. This behaviour suggests that sulphur species are mainly adsorbed reversibly on the Ni surface and can desorb once the contaminant is removed from the fuel stream, allowing the catalyst to recover its initial activity.

In the final stage of the experiment, DMS is reintroduced at 2.5 ppm and subsequently increased to 5 ppm. The same trend observed during the first contamination sequence is detected again: both P4 and P7 increase with respect to the clean baseline, confirming that fuel-electrode charge transfer and gas conversion remain the processes most sensitive to sulphur contamination. However, similarly to the earlier steps, the increase in P4 becomes less pronounced once the initial poisoning has occurred, while P7 continues to grow slightly with increasing contaminant concentration.

4.4. CNLS fitting

To complement the EIS and DRT analyses, the impedance spectra were also fitted by CNLS using the equivalent circuit described in Fig. 2. Differently from DRT approach, which aims at separating overlapping processes and assigning each peak to a specific physicochemical phenomenon, the CNLS analysis directly provides an estimate of the resistances associated with each contribution and a quantification of their evolution under DMS exposure.

Fig. 6 shows the fitted resistive trends of cell 3 and cell 4, which are the central cells of the stack. This choice was made to clearly show the trend of the most representative cells of the stack, to simplify the visualisation. Similar behaviours are found for the other cells.

As shown in Fig. 6a, the resistance related to the anode electrochemical process (R4) increases sharply upon the first DMS addition and then tends to level off as the contaminant concentration is further increased. This behaviour supports the hypothesis that the most active Ni sites are already affected during the initial exposure, so that subsequent sulphur addition produces only limited further changes in the intrinsic electrochemical kinetics. By contrast, the gas-conversion-related resistance (R7) continues to increase with contaminant concentration, indicating that the ability of the fuel electrode to maintain local chemical equilibrium becomes progressively more hindered as sulphur coverage rises.

The CNLS fit also highlights smaller variations in the remaining contributions. In particular, the low-frequency resistance (R8) associated with the slowest fuel-side relaxation process shows a moderate change during contamination and returns to its initial value after DMS removal, indicating that this contribution is also governed by reversible changes in catalytic activity and local gas composition. Similarly, the intermediate contribution R5 and R6 exhibits limited changes, suggesting that transport-related effects are secondary with respect to the dominant modifications in charge

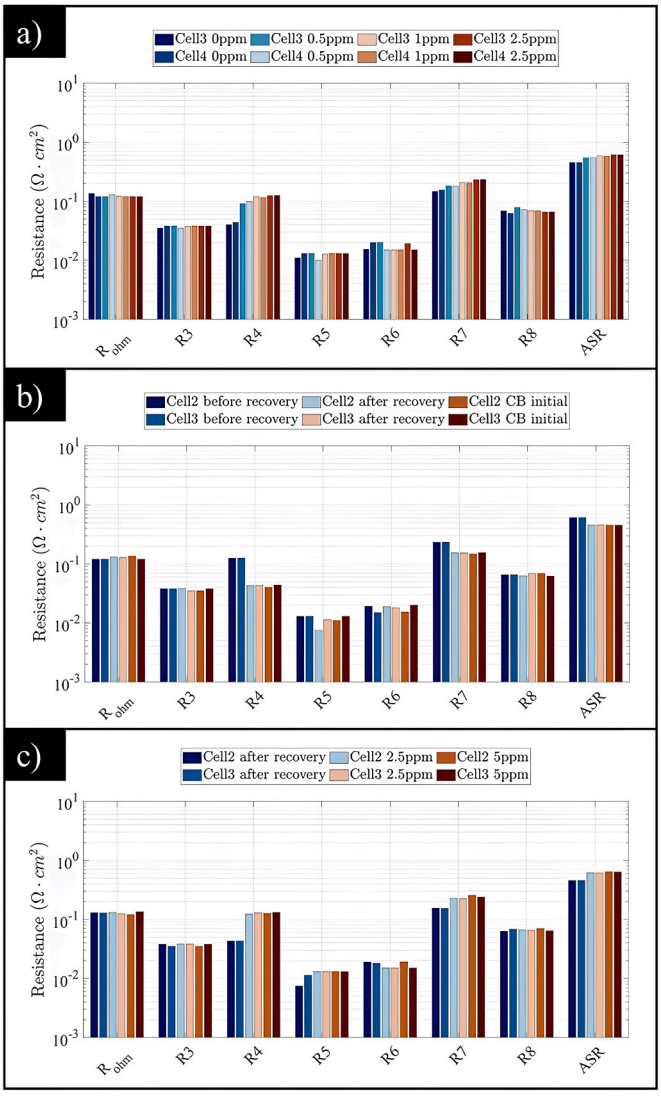

Fig. 6. Resistance of different elements from CNLS fit for a) 0.5,1,2 ppm DMS exposure b) recovery phase, c) 2.5, 5 ppm DMS exposure.

transfer and gas conversion. The highest frequency resistance (R3) and ohmic terms remain essentially unchanged throughout the tests, confirming that the electrolyte and cell hardware are not significantly affected by DMS in the investigated operating window.

An important outcome of the CNLS analysis is that, after the recovery phase (see Fig. 6b), all fitted resistances return close to their clean-baseline values. This quantitatively confirms the reversibility already suggested by both the voltage evolution and the DRT results, and indicates that the observed impedance increase originates mainly from reversible sulphur adsorption on the Ni catalyst, with no electrochemical signature of irreversible degradation detected within the investigated time window. This does not rule out subtle microstructural changes below the sensitivity of the electrochemical techniques used here, since no post-test characterisation was performed. In the final contamination sequence (Fig. 6c), the same pattern is recovered: the gas-conversion-related resistance continues to show the strongest sensitivity to increasing DMS concentration, whereas the charge-transfer term remains comparatively less affected once the initial poisoning has occurred. Overall, the CNLS results provide a consistent parameter-based confirmation of the mechanistic interpretation derived from DRT.

Figure S.5 in the Supplementary Information presents the characteristic time constants associated with each DRT peak under contamination and recovery conditions. The processes remain well separated over several orders of magnitude in relaxation time. While DMS exposure significantly affects peak amplitudes, the corresponding time constants remain largely unchanged, indicating that sulphur poisoning modifies the intensity of existing electrochemical and transport rather than the relaxation times. Fig S6 in Supplementary information shows instead the dispersion factor.

The present results are consistent with our previous investigation performed on a Ni-GDC electrolyte-supported single cell exposed to DMS under processed biogas conditions [24,25]. In both studies (see Table 4), DMS poisoning was found to be largely reversible following contaminant removal in both cell configurations. Despite these common trends, the present work significantly extends the previous single-cell investigation by demonstrating the behaviour of a six-cell short stack under realistic operating conditions. In particular, the stack configuration enables the analysis of spatial heterogeneity along the fuel-flow direction, revealing cell-to-cell differences in poisoning severity that cannot be captured in single-cell experiments. These results therefore bridge the gap between fundamental single-cell studies and practical stack operation.

4.5. Effect of sulphur poisoning

Hansen [36] proposed a relationship between SOFC performance degradation and the surface coverage of sulphur species on nickel. In his work, sulphur coverage was estimated through the Temkin-like isotherm originally proposed by Alstrup et al. [37], which describes the equilibrium adsorption of sulphur on Ni surfaces. According to this formulation, the sulphur coverage (θ_S) can be calculated as follows:

Table 4
Comparison between single cell and short stack work.

Feature	Yu et al. [24]	Present work
Cell architecture	Electrolyte-supported Ni-GDC	Anode supported Ni-YSZ
Device	Single cell	6-cell short stack
Fuel	Processed biogas	Processed biogas
Contaminant	DMS (+H_2S)	DMS
Main affected DRT processes	Gas conversion + O^{2-} surface exchange	Gas conversion + anode charge transfer
High-frequency processes	Nearly unchanged	Nearly unchanged
Reversibility	Nearly complete[a]	Nearly complete[a]

[a] Based on electrochemical recovery (voltage, EIS, DRT, CNLS); no post-test microstructural or phase characterisation was performed in either study.

$$\theta_S = 1.45 - 9.53 \cdot 10^{-5} T + 4.17 \cdot 10^{-5} T \cdot ln\left(\frac{p_{H_2S}}{p_{H_2}}\right) \quad (3)$$

When Eq. (3) is used to correlate the impact of sulphur on SOFC performance, it is essential to consider the actual partial pressures of hydrogen sulphide (p_{H_2S}) and hydrogen (p_{H_2}) at the TPB, together with the local operating temperature (T). These parameters determine the equilibrium between adsorbed sulphur species and the gas phase, which ultimately governs the fraction of Ni active sites blocked by sulphur.

However, when complex fuel mixtures are used, the effective hydrogen partial pressure is not always straightforward to determine. For this reason, Papurello et al. [38], working with biogas-fed SOFCs, introduced the concept of equivalent hydrogen partial pressure. In this approach, methane and carbon monoxide are considered additional hydrogen sources because they can be converted to hydrogen within the fuel electrode through reforming and water-gas shift reactions. Methane therefore counts as four hydrogen equivalents, while carbon monoxide contributes one. This correction provides a more realistic estimation of the reducing potential of the fuel mixture and of the effective hydrogen partial pressure governing sulphur adsorption. Using this methodology, they calculated the sulphur surface coverage and correlated it with the experimentally observed performance loss (P) according to the following relation:

$$P = k \cdot (\theta_S - \theta_{min}) \quad (4)$$

where θ_{min} represents a minimum threshold coverage below which the performance drop is negligible.

A similar approach was adopted by Madi et al. [22] to evaluate the impact of thiophene (C_4H_4S) on Ni-YSZ SOFC anodes. In that study, Eq. (3) was also used to estimate sulphur surface coverage, based on the assumption that thiophene decomposes under SOFC operating conditions to form hydrogen sulphide, which then acts as the actual poisoning species.

Following the same rationale, the Temkin-type framework can also be applied to DMS contamination. Although DMS is not itself hydrogen sulphide, previous gas chromatography (GC) measurements performed within our research group under the same processed biogas conditions showed that DMS is almost completely converted into H_2S at SOFC operating temperatures, with no measurable residual DMS detected within the experimental uncertainty (see Supplementary Materials Figure S.7.). This observation is further supported by the decomposition pathway proposed by Yu et al. [24], who indicates that DMS decompose or reform at SOFC operating temperatures on Ni-based catalysts, ultimately producing H_2S as the predominant sulphur-containing species. The present approach therefore assumes that DMS conversion is sufficiently fast compared with the gas residence time, so that the local H_2S partial pressure can be reasonably approximated by the equilibrium value throughout the stack. Although local deviations from this assumption, particularly in the inlet region, cannot be completely excluded due to spatial concentration gradients, they are expected to be limited under the investigated operating conditions. Therefore, under the operating conditions investigated in the present work, sulphur poisoning is expected to be governed by H_2S adsorption on the Ni surface. On this basis, the equilibrium sulphur coverage can be reasonably estimated using the Temkin-type isotherm originally developed for H_2S. Accordingly, Eq. (3) is employed to estimate the equilibrium sulphur surface coverage associated with the investigated DMS concentrations and to correlate it with the experimentally observed performance losses. The calculated equilibrium sulphur coverage should therefore be interpreted as a model-derived estimate, obtained under the assumption of complete DMS conversion to H_2S, rather than as a directly measured surface quantity.

In the present study, the effective hydrogen partial pressure used in Eq. (3) is not taken directly from the inlet composition but is instead derived from the expected gas composition along the fuel electrode under the operating conditions of the stack. During SOFC operation, the

electrochemical consumption of hydrogen continuously modifies the gas composition between the inlet and outlet of the anode channel. As a consequence, the hydrogen partial pressure at the triple phase boundary cannot be accurately represented by the inlet value alone. To obtain a more representative value, the inlet hydrogen partial pressure $p_{H_2,in}$ was calculated from the feed composition, while the outlet hydrogen partial pressure $p_{H_2,out}$ was estimated using thermodynamic equilibrium calculations performed with Cantera under the same operating conditions. The effective hydrogen partial pressure was then approximated using the geometric mean of the inlet and outlet values:

$$p_{H_2,eff} = \sqrt{p_{H_2,in} \cdot p_{H_2,out}} \tag{5}$$

This formulation is equivalent to taking the average of the logarithms of the partial pressures along the anode channel and is consistent with the logarithmic dependence appearing in the Temkin adsorption isotherm. Since Eq. (3) contains the term $\ln\left(p_{H_2S}/p_{H_2}\right)$, the geometric mean provides a physically meaningful estimate of the hydrogen partial pressure experienced by the catalyst surface along the electrode. In other words, it approximates the average thermodynamic driving force governing sulphur adsorption in a system where the gas composition varies continuously along the flow path. This approach therefore offers a more realistic estimation of the effective reducing environment at the fuel electrode compared to using either the inlet or outlet value alone. For completeness, the Supplementary Information includes a plot of sulphur coverage versus contaminant concentration comparing the two procedures used to define $p_{H_2,eff}$. Specifically, the curve obtained with the method proposed by Papurello et al. [38] is shown alongside the one derived using the present approach based on the geometric mean of inlet and outlet hydrogen partial pressures. Both methods yield nearly identical trends, with the present approach predicting slightly higher sulphur coverages (corresponding to a difference below 6%).

In line with previous studies, also in this work a strong linear correlation was found between the relative performance drop P and the sulphur coverage calculated using the Temkin-like expression. The performance loss data were fitted using Eq. (4), where $\theta_{\min}$ represents a minimum threshold coverage below which the performance drop is negligible. Under the specific operating conditions and modelling assumptions of this study, the regression yields $\theta_{\min} \approx 0.678$ ($R^2 = 0.9964$). This value should be regarded as a preliminary, model-dependent correlation rather than a generalisable diagnostic threshold, given that it relies on an assumed complete DMS-to-H_2S conversion and an approximated effective H_2 partial pressure rather than direct TPB measurements (Fig. 7a). The introduction of θ_{min} is physically meaningful. It suggests that a finite fraction of the Ni surface can be covered by sulphur species without producing a measurable impact on cell performance. This behaviour is consistent with the existence of active-site heterogeneity on Ni surfaces, where less active or geometrically less relevant sites may be poisoned first, while the sites governing charge transfer remain initially unaffected. Only when the sulphur coverage exceeds this critical value, the blockage begins to significantly interfere with electrochemical fuel oxidation, resulting in a detectable voltage drop. By inverting the Temkin-like expression, the corresponding DMS concentration associated with θ_{min} was estimated as $C_{\lim} \approx 0.081$ ppm under the present operating conditions. This value represents the predicted DMS concentration below which sulphur poisoning is not expected to induce measurable performance degradation. The identification of such a threshold is particularly relevant from an operational standpoint. Since this value lies below the lowest experimentally investigated concentration (0.5 ppm), it represents a model-based extrapolation rather than an experimentally validated tolerance limit. This extrapolated value should not be interpreted as an experimentally validated tolerance limit or as a stack-scale diagnostic criterion. It is reported here only to illustrate the qualitative trend predicted by the model within the investigated operating window; quantitative use of this threshold requires dedicated sub-ppm experiments and, ideally, direct TPB gas-composition measurements.

The computed values of θ_S were plotted against the inlet DMS concentration. Since the Temkin-like formulation is logarithmic in the contaminant-to-hydrogen partial pressure, the very low concentrations cannot be represented because of the mathematical singularity associated with $\ln(0)$. For plotting and interpolation purposes only, an additional "quasi-zero" concentration point was introduced ($1\ \text{ppb} = 10^{-3}$ ppm) as lower bound. At this concentration, sulphur coverage was assumed negligible, consistent with the absence of measurable voltage loss once cell had stabilised under contaminant-free operation. To provide a mapping within the investigated range, the concentration-coverage relationship was parameterised using in the following log-linear form:

$$\theta_S = a + b \ln\left(\frac{p_{\text{cont}}}{p_{H_2,eff}}\right) \tag{6}$$

where a and b are fitted coefficients for the present dataset. This parameterisation is not intended to represent a mechanistic adsorption isotherm for DMS; rather, it offers a practical interpolation tool that enables direct comparison between protocols and operating conditions, and facilitates the estimation of threshold concentrations once a performance-onset coverage index is identified from the P–θ_S correlation. The resulting curve shown in Fig. 7b exhibits a rapid increase at low concentration followed by a slower, logarithmic-like evolution at higher concentrations.

5. Conclusions

Clarifying the degradation and recovery behaviour of Ni-YSZ anode-supported cells in the presence of sulphur compounds is essential for advancing biogas-fed SOFC technology. In this work, dimethyl sulphide, a relevant sulphur species in biomass derived fuels, was investigated on a six-cell anode supported SOFC stack over a range of concentrations (0.5-5 ppm), providing stack scale evidence that sulphur compounds other than H_2S can be detrimental even at the ppm level. The combination of KK-validated EIS, DRT reconstruction and ECM fitting enabled separation

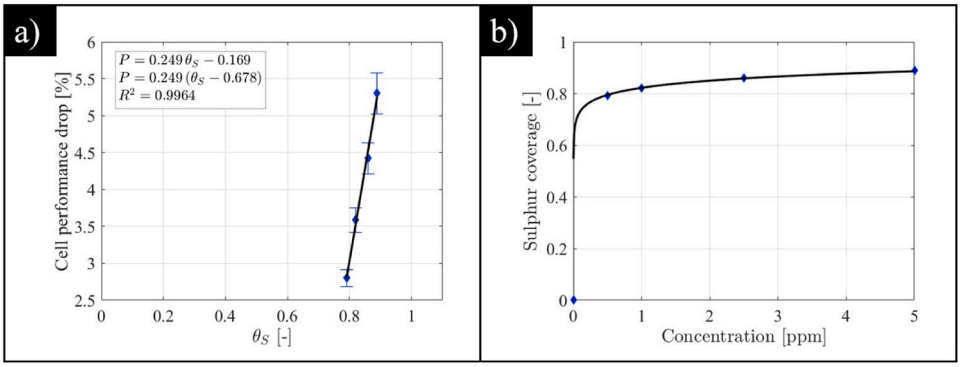

Fig. 7. a) Performance drop versus sulphur coverage calculated through Temkin-like isotherm; b) Concentration versus sulphur coverage to obtain new isotherm.

of the main contributions to performance loss and provided operando descriptors of DMS-induced changes. The EIS and DRT analyses shows that the dominant impact of DMS is consistently observed in the anode-related contributions, particularly in the charge transfer and gas conversion processes.

Two distinct degradation behaviours were identified: (1) a rapid exponential performance drop upon DMS introduction and (2) a slower but continuous degradation with a comparatively low rate.

The strongest changes were consistently associated with the anode charge transfer and gas conversion contributions, suggesting that DMS primarily affects the availability of electrochemically active Ni-sites and the local gas chemistry at the anode (e.g., reforming/WGS-related pathways). DMS is known to thermally decompose at SOFC operating temperatures even in inert environments, indicating that its primary cracking is not inherently dependent on electrochemical operation. However, as shown in the EIS and DRT results, under polarised conditions the local gas composition at the anode changes due to fuel consumption and steam formation, leading to a more H_2-depleted and locally oxidising environment. Such shifts may modify sulphur speciation and adsorption equilibria. The degradation behaviour observed under load therefore likely reflects a dynamic balance between sulphur adsorption and gas-phase speciation.

Upon contaminant removal, recovery of the measured resistive contributions was observed between the two 2.5 ppm exposures, indicating that, within the tested duration, the dominant component of DMS poisoning is reversible at the electrochemical level. A comparable voltage recovery was also observed following the final 5 ppm exposure, although this phase was not characterised by EIS, so complete reversibility at this concentration cannot be confirmed.

Finally, an effective sulphur coverage index was evaluated by adapting Temkin-like formulations commonly used for H_2S. The performance-coverage correlation suggests an onset coverage θ_{min} equal to 0.678 below which the performance drop is negligible and provides an operating point which defines the contaminant threshold, offering a compact framework to compare protocols and conditions. Future work should extend exposure times and, where relevant, concentration windows to assess the emergence of irreversible effects, and combine electrochemical analysis with gas-phase speciation to better constrain the DMS-to-(H_2S/COS) conversion pathways and refine a DMS-specific coverage model across temperature, fuel utilisation, and current density.

CRediT authorship contribution statement

Lucia Pera: Conceptualization, Data curation, Formal analysis, Investigation, Visualization, Writing – original draft. **Audrey Wesoly:** Data curation. **Stefan Diethelm:** Data curation, Writing – review & editing. **Cédric Frantz:** Conceptualization, Data curation, Formal analysis, Investigation, Methodology, Visualization, Writing – review & editing. **Hangyu Yu:** Conceptualization, Data curation, Formal analysis, Investigation, Methodology, Software, Visualization, Writing – review & editing. **Marta Gandiglio:** Supervision, Writing – review & editing. **Paolo Marocco:** Supervision, Writing – review & editing. **Massimo Santarelli:** Funding acquisition, Supervision. **Jan Van Herle:** Funding acquisition, Supervision.

Declaration of competing interests

The authors declare that they have no known competing financial interests or personal relationships that could have appeared to influence the work reported in this paper.

Acknowledgements

The work is supported by the Fuel Cells and Hydrogen Joint Undertaking, Belgium under grant agreement No 826234 (Waste2Watts) and No 24.00185 - 101146861 (Niagara), which receive support from the European Union's Horizon 2020 research and innovation programme.

During the preparation of this work the authors used *ChatGPT,* OpenAI, (2026) in order to rephrase and improve the clarity and flow of the text. After using this tool, the authors reviewed and edited the content as needed and take full responsibility for the content of the published article.

Acronyms

ASR	Area specific resistance
AU	Air utilisation
CB	Cold biogas recirculation
CNLS	Complex non linear square
COS	Carbonyl sulphide
DMS	Dimethyl sulphide
DRT	Distribution relaxation times
ECM	Equivalent circuit model
ESC	Electrolyte supported cell
EIS	Electrochemical impedance spectroscopy
FU	Fuel utilisation
GC	Gas chromatography
GDC	Gadolinium doped ceria
KK	Kramers-Kronig
MFC	Mass flow controller
OCV	Open circuit voltage
SOFC	Solid oxide fuel cell
TPB	Triple phase boundary
UPS	Uninterrupted power supply
WGS	Water gas shift
YSZ	Yttria stabilised zirconia

Appendix A. Supplementary data

Supplementary data to this article can be found online at https://doi.org/10.1016/j.jpowsour.2026.241255.

Data availability

Data will be made available on request.

References

[1] M. Singh, D. Zappa, E. Comini, Solid oxide fuel cell: decade of progress, future perspectives and challenges, Int. J. Hydrogen Energy 46 (2021) 27643–27674, https://doi.org/10.1016/j.ijhydene.2021.06.020.

[2] Van herle Jan, Y. Membrez, O. Bucheli, Biogas as fuel source for SOFC co-generators, J. Power Sources 127 (1-2) (2004) 300–312.

[3] M. Gandiglio, A. Lanzini, M. Santarelli, M. Acri, T. Hakala, M. Rautanen, Results from an industrial size biogas-fed SOFC plant (the DEMOSOFC project), Int. J. Hydrogen Energy 45 (2020) 5449–5464, https://doi.org/10.1016/j.ijhydene.2019.08.022.

[4] H. Langnickel, M. Rautanen, M. Gandiglio, M. Santarelli, T. Hakala, M. Acri, J. Kiviaho, Efficiency analysis of 50 kWe SOFC systems fueled with biogas from waste water, J. Power Sources Adv. 2 (2020), https://doi.org/10.1016/j.powera.2020.100009.

[5] A.O. Omosun, A. Bauen, N.P. Brandon, C.S. Adjiman, D. Hart, Modelling system efficiencies and costs of two biomass-fuelled SOFC systems, J. Power Sources 131 (2004) 96–106, https://doi.org/10.1016/j.jpowsour.2004.01.004.

[6] M.T. Mehran, M.Z. Khan, R.H. Song, T.H. Lim, M. Naqvi, R. Raza, B. Zhu, M. B. Hanif, A comprehensive review on durability improvement of solid oxide fuel cells for commercial stationary power generation systems, Appl. Energy 352 (2023), https://doi.org/10.1016/j.apenergy.2023.121864.

[7] L. Pera, M. Gandiglio, P. Marocco, D. Pumiglia, M. Santarelli, Trace contaminants in biogas: biomass sources, variability and implications for technology applications, J. Environ. Chem. Eng. 12 (2024), https://doi.org/10.1016/j.jece.2024.114478.

[8] A. Calbry-Muzyka, H. Madi, F. Rüsch-Pfund, M. Gandiglio, S. Biollaz, Biogas composition from agricultural sources and organic fraction of municipal solid waste, Renew. Energy 181 (2022) 1000–1007, https://doi.org/10.1016/j.renene.2021.09.100.

[9] J.F.B. Rasmussen, A. Hagen, The effect of H2S on the performance of Ni-YSZ anodes in solid oxide fuel cells, J. Power Sources 191 (2009) 534–541, https://doi.org/10.1016/j.jpowsour.2009.02.001.

[10] G. Pongratz, V. Subotić, H. Schroettner, C. Hochenauer, M. Skrzypkiewicz, J. Kupecki, A. Anca-Couce, R. Scharler, Analysis of H2S-related short-term degradation and regeneration of anode- and electrolyte supported solid oxide fuel cells fueled with biomass steam gasifier product gas, Energy 218 (2021), https://doi.org/10.1016/j.energy.2020.119556.

[11] D. Papurello, R. Borchiellini, P. Bareschino, V. Chiodo, S. Freni, A. Lanzini, F. Pepe, G.A. Ortigoza, M. Santarelli, Performance of a solid oxide fuel cell short-stack with biogas feeding, Appl. Energy 125 (2014) 254–263, https://doi.org/10.1016/j.apenergy.2014.03.040.

[12] M.T. Mehran, M.Z. Khan, S.B. Lee, T.H. Lim, S. Park, R.H. Song, Improving sulfur tolerance of Ni-YSZ anodes of solid oxide fuel cells by optimization of microstructure and operating conditions, Int. J. Hydrogen Energy 43 (2018) 11202–11213, https://doi.org/10.1016/j.ijhydene.2018.04.200.

[13] O. Gohar, M.Z. Khan, M. Saleem, O. Chun, Z.U.D. Babar, M.M.U. Rehman, A. Hussain, K. Zheng, J.H. Koh, A. Ghaffar, I. Hussain, E. Filonova, D. Medvedev, M. Motola, M.B. Hanif, Navigating the future of solid oxide fuel cell: comprehensive insights into fuel electrode related degradation mechanisms and mitigation strategies, Adv. Colloid Interface Sci. 331 (2024), https://doi.org/10.1016/j.cis.2024.103241.

[14] A. Hagen, J.F.B. Rasmussen, K. Thydén, Durability of solid oxide fuel cells using sulfur containing fuels, J. Power Sources (2011) 7271–7276, https://doi.org/10.1016/j.jpowsour.2011.02.053.

[15] A. Hauch, A. Hagen, J. Hjelm, T. Ramos, Sulfur poisoning of Ni/Stabilized-Zirconia anodes – effect on long-term durability, ECS Trans. 57 (2013) 615–625, https://doi.org/10.1149/05701.0615ecst.

[16] A. Weber, S. Dierickx, A. Kromp, E. Ivers-Tiffée, Sulfur poisoning of anode-supported SOFCs under reformate operation, Fuel Cells 13 (2013) 487–493, https://doi.org/10.1002/fuce.201200180.

[17] K. Sasaki, K. Susuki, A. Iyoshi, M. Uchimura, N. Imamura, H. Kusaba, Y. Teraoka, H. Fuchino, K. Tsujimoto, Y. Uchida, N. Jingo, H[sub 2]S poisoning of solid oxide fuel cells, J. Electrochem. Soc. 153 (2006) A2023, https://doi.org/10.1149/1.2336075.

[18] A. Lanzini, H. Madi, V. Chiodo, D. Papurello, S. Maisano, M. Santarelli, J. Van herle, Dealing with fuel contaminants in biogas-fed solid oxide fuel cell (SOFC) and molten carbonate fuel cell (MCFC) plants: degradation of catalytic and electrocatalytic active surfaces and related gas purification methods, Prog. Energy Combust. Sci. 61 (2017) 150–188, https://doi.org/10.1016/j.pecs.2017.04.002.

[19] D. Papurello, A. Lanzini, D. Drago, P. Leone, M. Santarelli, Limiting factors for planar solid oxide fuel cells under different trace compound concentrations, Energy 95 (2016) 67–78, https://doi.org/10.1016/j.energy.2015.11.070.

[20] A. Ishikura, S. Sakuno, N. Komiyama, H. Sasatsu, N. Masuyama, H. Itoh, K. Yasumoto, Influence of H2S poisoning on anode layer of SOFC, ECS Trans. 7 (2007) 845–850, https://doi.org/10.1149/1.2729174.

[21] F.P. Nagel, T.J. Schildhauer, J. Sfeir, A. Schuler, S.M.A. Biollaz, The impact of sulfur on the performance of a solid oxide fuel cell (SOFC) system operated with hydrocarboneous fuel gas, J. Power Sources 189 (2009) 1127–1131, https://doi.org/10.1016/j.jpowsour.2008.12.092.

[22] H. Madi, S. Diethelm, C. Ludwig, J. Van Herle, Organic-sulfur poisoning of solid oxide fuel cell operated on bio-syngas, Int. J. Hydrogen Energy 41 (2016) 12231–12241, https://doi.org/10.1016/j.ijhydene.2016.06.014.

[23] L. Pera, M. Gandiglio, P. Marocco, D. Pumiglia, L. Della Seta, M. Santarelli, Impact of trace contaminants on SOFC operated with bio-syngas: sulphur and siloxane-induced degradation, J. Power Sources 665 (2026) 238967, https://doi.org/10.1016/j.jpowsour.2025.238967.

[24] H. Yu, C. Frantz, L. Savioz, P. Aubin, D. Fronterotta, C. Geipel, H. Moussaoui, G. Jeanmonod, L. Wang, J. Van herle, Poisoning and recovery behavior of Ni-GDC based electrolyte-supported solid oxide fuel cell exposed to common sulfur compounds under processed biogas environment, J. Power Sources 642 (2025), https://doi.org/10.1016/j.jpowsour.2025.236901.

[25] L. Pera, C. Frantz, H. Yu, M. Gandiglio, P. Marocco, M. Santarelli, J. Van Herle, Electrochemical performance and degradation behaviour of Ni–YSZ anode-supported SOFC operated with pre-processed biogas, Electrochim. Acta 568 (2026), https://doi.org/10.1016/j.electacta.2026.148838.

[26] H. Langnickel, A. Hagen, New methodology of studying H 2 S poisoning effects on SOFC's fueled by carbon containing fuels like biogas, ECS Trans. 91 (2019) 511–521, https://doi.org/10.1149/09101.0511ecst.

[27] H. Yu, C. Frantz, L. Savioz, D. Fronterotta, P. Aubin, C. Geipel, H. Moussaoui, G. Jeanmonod, L. Wang, J. Van herle, Parametric study of Ni-GDC based electrolyte-supported cell via electrochemical impedance spectroscopy, Appl. Energy 415 (2026) 127941, https://doi.org/10.1016/j.apenergy.2026.127941.

[28] B.A. Boukamp, Distribution (function) of relaxation times, successor to complex nonlinear least squares analysis of electrochemical impedance spectroscopy? JPhys Energy 2 (2020) https://doi.org/10.1088/2515-7655/aba9e0.

[29] Katsuhiko Ogata, Modern Control Engineering, fifth ed., Prentice Hall, 2022.

[30] Powell Franklin, Emami-Naeini, Feedback Control of Dynamic Systems, eighth ed., 2020.

[31] M.Z. Khan, M. Saleem, M.B. Hanif, J.H. Koh, I. Hussain, U. Gulshan, S. Latif, H. Liang, A. Ghaffar, I. Shakir, B. Lin, Advanced electrochemical impedance spectroscopy for high-performance solid oxide fuel cells: a critical review, Appl. Energy 407 (2026), https://doi.org/10.1016/j.apenergy.2025.127347.

[32] A. Hauch, A. Hagen, J. Hjelm, T. Ramos, Sulfur poisoning of SOFC anodes: effect of overpotential on long-term degradation, J. Electrochem. Soc. 161 (2014) F734–F743, https://doi.org/10.1149/2.080406jes.

[33] D. Montinaro, A.R. Contino, A. Dellai, M. Rolland, Determination of the impedance contributions in anode supported solid oxide fuel cells with (La,Sr)(Co,Fe)O3-δ cathode, Int. J. Hydrogen Energy 39 (2014) 21638–21646, https://doi.org/10.1016/j.ijhydene.2014.09.081.

[34] P. Caliandro, A. Nakajo, S. Diethelm, J. Van herle, Model-assisted identification of solid oxide cell elementary processes by electrochemical impedance spectroscopy measurements, J. Power Sources 436 (2019), https://doi.org/10.1016/j.jpowsour.2019.226838.

[35] Z. Wuillemin, Y. Antonetti, C. Beetschen, O. Millioud, S. Ceschini, H. Madi, J. Van herle, Local activation and degradation of electrochemical processes in a SOFC, ECS Trans. 57 (2013) 561–570, https://doi.org/10.1149/05701.0561ecst.

[36] J.B. Hansen, Correlating sulfur poisoning of SOFC nickel anodes by a temkin isotherm, Electrochem. Solid State Lett. 11 (2008), https://doi.org/10.1149/1.2960521.

[37] I. Alstrup, J.R. Rostrup-Nielsen, S. Røen, High temperature hydrogen sulfide chemisorption on nickel catalysts, Appl. Catal. 1 (5) (1981) 303–314.

[38] D. Papurello, A. Lanzini, S. Fiorilli, F. Smeacetto, R. Singh, M. Santarelli, Sulfur poisoning in Ni-anode solid oxide fuel cells (SOFCs): deactivation in single cells and a stack, Chem. Eng. J. 283 (2016) 1224–1233, https://doi.org/10.1016/j.cej.2015.08.091.